GEOLOGY

Obliquity disruption and Antarctic ice sheet dynamics over a 2.4-Myr astronomical grand cycle

Nicholas B. Sullivan[1,2]*, Stephen R. Meyers[1], Richard H. Levy[3,4], Robert M. McKay[3], Tina van de Flierdt[5], James Marschalek[5], Matteo Perotti[6], Luca Zurli[6], Franco Talarico[6]†, David Harwood[7], Laura De Santis[8], Fabio Florindo[9], Tim R. Naish[3], Georgia R. Grant[4], Molly O. Patterson[10], Expedition 374 scientists‡

Marine $\delta^{18}O$ data reveal astronomical forcing of the climate and cryosphere during the Miocene, when atmospheric P_{CO_2} was on par with emissions scenarios over the next century. This inspired hypotheses for how Milankovitch cycles, ice-ocean interactions, and greenhouse gases influence ice volume. Mass balance controls for marine and terrestrial ice sheets differ, and proxy data collected far from Antarctica provide valuable but limited insight into regional processes. We evaluate clast abundance data from Antarctic marine sedimentary records, observing a strong signal of eccentricity and precession coincident with a terrestrial ice sheet and a clear obliquity signal at the margins of a marine ice sheet. These analyses are integrated with a synthesis of proxy data, and we argue that high variance in obliquity forcing (mediated and enhanced by the ocean and atmosphere) can inhibit ice sheet growth, even when insolation forcing is conducive to glaciation. This "obliquity disruption" explains cryosphere variability before the existence of large northern hemisphere ice sheets.

INTRODUCTION

The response of Antarctic ice sheets (AISs) and the Southern Ocean to climate change is complex, nonlinear, and uncertain (*1*–*4*), making it challenging to predict the cryosphere's response to a warming world (*1*, *5*–*7*). Paleoclimate investigations provide essential insights for understanding cryospheric variability. Although the best-constrained paleoclimate records derive primarily from the Quaternary and Pliocene (*8*–*10*), projected warming could surpass the warmest climates of these geologic intervals within decades (*11*). In this study, we conduct a detailed analysis on links between astronomical forcing and the Antarctic cryosphere during the Early Miocene (Burdigalian), between 16 and 20 million years ago (Ma). While not a direct analog, this time interval is an informative example of a climate state similar to the one emerging via anthropogenic influence (*11*), with global mean surface temperatures 3° to 4°C warmer than today (*12*) and atmospheric P_{CO_2} (partial pressure of CO_2) concentrations projected to exceed 500 parts per million (ppm) (*13*–*17*).

Antarctica's ice sheets experienced dynamic changes in volume and extent during the Early Miocene Burdigalian Age (*18*–*20*). The East Antarctic Ice Sheet (EAIS), like today, was predominantly grounded on land above sea level, but unlike the present, large regions of the West Antarctic Ice Sheet (WAIS) were also grounded on land (*21*). The West Antarctic landmass deepened during the Neogene as tectonic rifting drove crustal subsidence and glacial erosion removed rock and sediment from the continental interior (*19*). At some times during the Early Miocene, both ice sheets retreated inland from their coastlines, while at other times they advanced into marine environments across the continental shelf (*19*, *22*–*24*) (Fig. 1). These alternations between terrestrial ice sheets and larger ice sheets with substantial marine-based regions drove eustatic change on the order of 35 to 40 m, as documented from far-field records of sea-level variability (*22*, *25*–*28*).

The dominant behavior of the AIS under these different configurations ("terrestrial" versus "terrestrial + marine") can be inferred from sedimentological and stratigraphic information collected from ice-proximal geologic records around the Antarctic margin (*19*, *22*, *29*–*32*). However, repeated scouring and erosion of the continental shelf by advancing glaciers makes reconstructing this history on astronomical timescales [~15 to 500 thousand years (kyr)] challenging in ice-proximal localities. Coupled climate and ice sheet modeling studies provide key insights and show that ice sheets could expand or retreat across widespread regions of Antarctica under Early Miocene climate conditions (*33*–*35*).

Another common approach is to infer the history of climate and AIS dynamics from distal deep-ocean benthic foraminiferal $\delta^{18}O$ records (*18*, *36*–*38*), which show strong evidence of astronomical forcing (*37*). Levy *et al.* (*39*) used a $\delta^{18}O$ megasplice (*40*) to evaluate changes in ice sheet behavior by estimating $\delta^{18}O$ "obliquity sensitivity" (S_{obl}), which is the ratio of observed obliquity-band variance in the $\delta^{18}O$ megasplice and the variance in the theoretical obliquity solution (*41*). Comparing S_{obl} with ice-proximal stratigraphic and seismic evidence for ice sheet extent led those authors to conclude that intervals of high S_{obl} in the Oligocene to Late Miocene coincided with times when extensive regions of Antarctica's ice sheets expanded into marine environments. In contrast, times of low S_{obl} coincided with contracted, predominantly terrestrial ice sheets. This is because terrestrial ice sheets are more directly influenced by local insolation during the summer melt season, which is controlled by precession (modulated by eccentricity) with moderate contribution from obliquity (*42*, *43*) [although see also (*44*)].

---

[1]Department of Geoscience, University of Wisconsin–Madison, Madison, WI 53706, USA. [2]Earth and Environmental Systems Institute, Pennsylvania State University, University Park, PA 16802, USA. [3]Antarctic Research Centre, Victoria University of Wellington, Wellington, New Zealand. [4]GNS Science, Lower Hutt, New Zealand. [5]Department of Earth Science and Engineering, Imperial College London, Exhibition Road, London SW7 2AZ, UK. [6]Department of Physical, Earth and Environmental Sciences, University of Siena, via Laterina 8, 53100 Siena, Italy. [7]Department of Earth and Atmospheric Sciences, University of Nebraska–Lincoln, Lincoln, NE 68588, USA. [8]National Institute of Oceanography and Applied Geophysics OGS, 34010 Sgonico TS, Italy. [9]Istituto Nazionale di Geofisica e Vulcanologia, Via di Vigna Murata, 605, 00143 Rome, Italy. [10]Department of Earth Sciences, Binghamton University, Binghamton, NY 13902, USA.
*Corresponding author. Email: nbs16@psu.edu
†Deceased.
‡Expedition 374 authors, collaborators, and affiliations are listed in the supplementary materials.

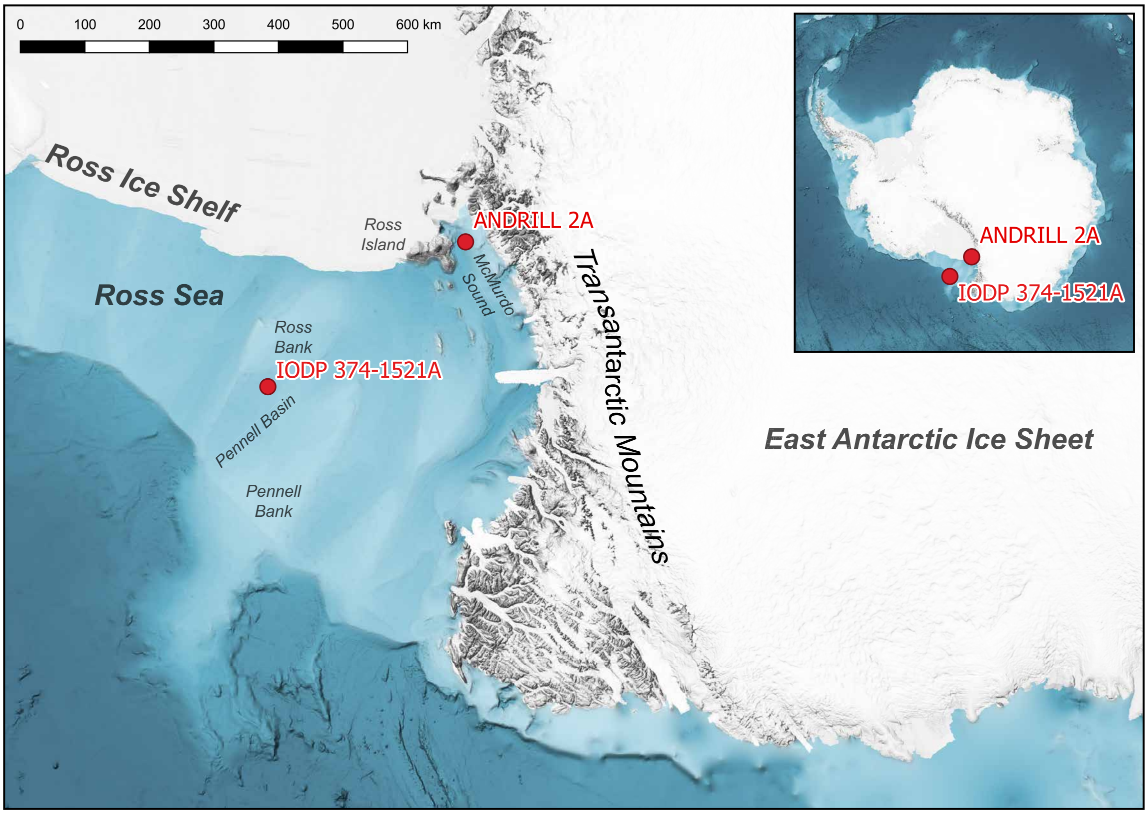

Fig. 1. Map of the localities in the Ross Sea and surrounding regions of Antarctica. Individual study sites are shown in red, and key regions in the vicinity are in gray text. Maps are based primarily on data from "Quantarctica" (*99*) and from the International Bathymetric Chart of the Southern Ocean (*100*).

Conversely, marine ice sheets should have an enhanced response to obliquity (*39*, *45*) due to the influence that Earth's obliquity has on meridional climate gradients (*2*), oceanic circulation (*46*), and poleward heat transport (*47*, *48*).

In an investigation of glaciomarine sequences from the Ross Sea, Naish *et al.* (*45*) argued that observed 41-kyr cyclicity in ice sheet behavior was linked to upwelling of warm deep water from the Southern Ocean, primarily forced by wind-induced Ekman pumping. This process is linked to obliquity variability through meridional shifts in the position of the Westerlies, which are influenced by meridional climate gradients (*49*).

These observations were invoked by Levy *et al.* (*39*) to explain enhanced S_{obl} at times of expanded, marine-terminating ice sheets. Here, we directly constrain the relationship between Milankovitch forcing, climate change, and the behavior of the AIS by examining AIS-proximal sedimentological data from the Ross Sea region of the Southern Ocean. We focus on an interval of the Early Miocene between ~16 Ma and ~20 Ma, through the evaluation of lithic clast abundance data from two drill cores: Antarctic Drilling (ANDRILL or AND) Site 2A from the McMurdo Sound and International Ocean Discovery Project (IODP) Expedition 374 Site U1521A from the Ross Sea (Fig. 1). The study sections at these two sites represent rare "stratigraphic windows" of relatively continuous, climate-sensitive sedimentation that permit quantitative characterization of astronomically influenced climate and cryosphere variability in proximal Antarctic environments.

Sediment clast abundance in glaciomarine strata has been linked to fluctuations of the ice sheet margin due to grounding zone advance and retreat, and increased ice-rafted debris flux at times of increased discharge of ice sheets into polar seas (*24*, *50*). Clast abundance may also be modulated by the depositional rate of glaciomarine mud, which dilutes clasts and varies in proportion with distance from ice sheet grounding lines (*51*). Previous work on downhole logging data (*32*) and mud content in Miocene strata in the Southern Ocean suggests that cyclic variability in clast abundance may be linked to astronomical forcing. However, analyses of high-resolution clast datasets through intervals with robust and independent age constraints are rare but nonetheless are required to better assess the relationship between external climate forcing and ice sheet variability.

To address this knowledge gap, we (i) evaluate potential astronomical signals in clast abundance data (Fig. 2) using an optimization approach (*52*) that explicitly considers uncertainty about timescale and astronomical response, (ii) assess their relationship to the marine δ^{18}O record and multi–million year (Myr) ("grand") cycles that modulate the amplitude of shorter Milankovitch periods (*41*, *53*), and (iii) integrate these results with globally dispersed proxy data and ice-proximal stratigraphic records to construct a model for AIS behavior (Fig. 3). We consider a model that is driven by interactions between astronomical forcing and the ocean-cryosphere system, augmented by glacial sedimentary processes, isostatic response of the lithosphere to sediment loading and glacial advance and retreat, and atmospheric CO_2 concentration (Fig. 4).

For this analysis, we sought ice-proximal stratigraphic records that preserve relatively continuous deposition at astronomical timescales. These conditions are rare in ice-proximal localities, but they

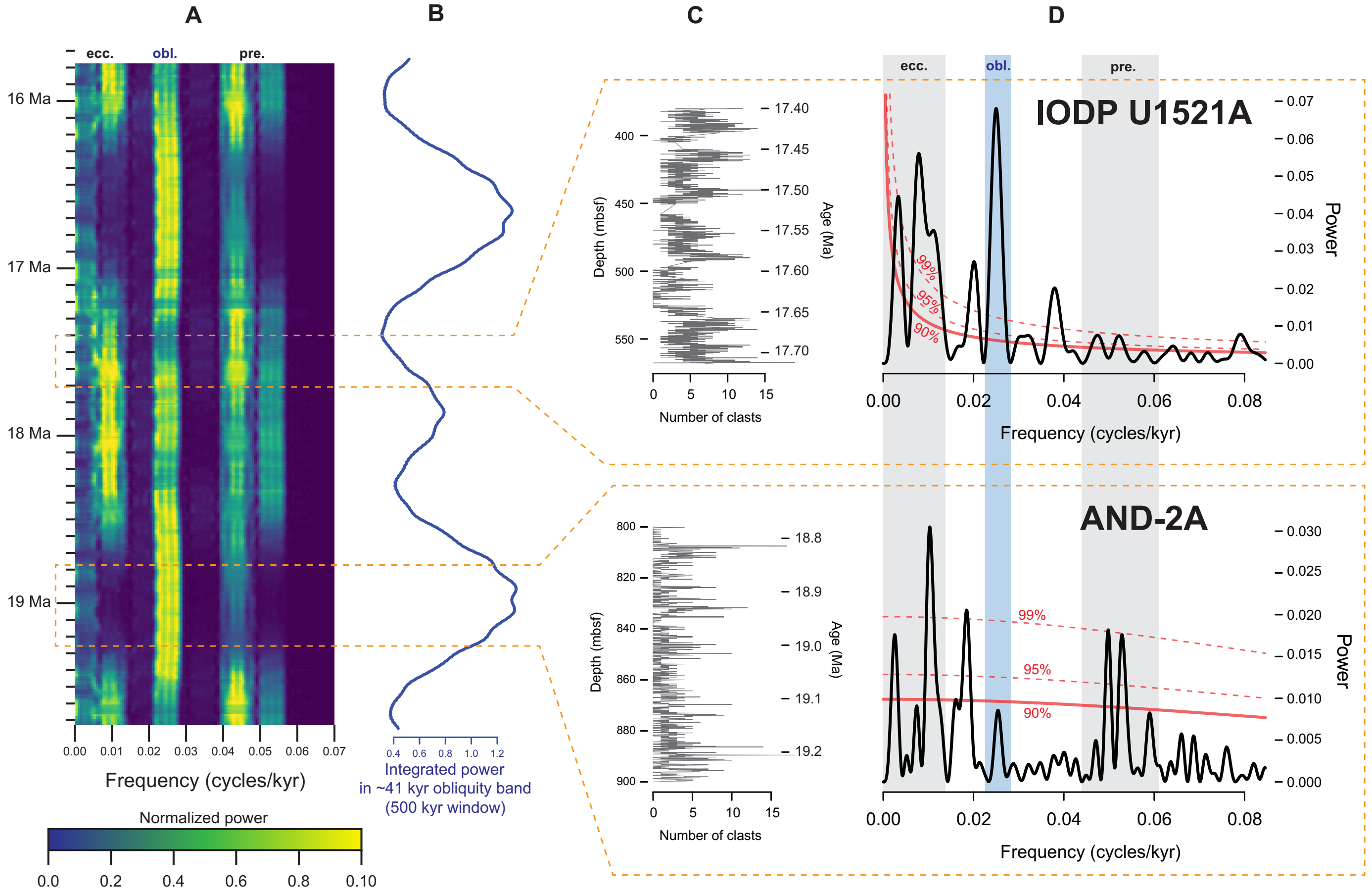

Fig. 2. Summary of results from proximal Antarctic sections in the Ross Sea. (**A**) An evolutive power spectrum analysis of normalized eccentricity-tilt-precession (ETP) through the early Miocene (*41*, *101*). (**B**) Integrated power over a 500-kyr window for the ~41-kyr obliquity bandwidth through the ETP solution. (**C**) Raw clast abundance data through the two study intervals at IODP U1521A (above) and AND-2A (below). Reported depth in meters below seafloor (mbsf) are shown on the left side of the graph, and the calibrated age model interpretations derived from TimeOpt corresponding to the data are shown on the right. (**D**) Power spectra for the age-calibrated clast abundance data derived from TimeOpt from both sites, and their associated red noise confidence levels. The predicted early Miocene eccentricity, obliquity, and precession bandwidth ranges are shown by gray shading.

occur at two locations in the Ross Sea region of Antarctica (Fig. 1). The first, AND-2A, is located on the inner continental shelf approximately 40 km offshore of the modern EAIS margin. A 100-m-thick mud-rich interval spanning 800 to 900 m in AND-2A represents a time when the grounding zone of the EAIS remained distal to the drill site for an extended period. While its margin episodically terminated in the marine environment, the majority of the ice sheet was terrestrial at this time (*24*). Published geochronology constrains this mud-rich interval to a time of exceptionally low eccentricity-precession variance (a "node") in the 2.4-Myr grand cycle (Figs. 2A and 3A) (*24*, *54*, *55*). This also coincides with a time of maximum obliquity variance in the theoretical astronomical solution (Figs. 2B and 3B), while observed δ^{18}O S_{obl} is low (Fig. 3D) (*24*, *39*).

The second locality is IODP Site U1521A, which is situated on the outer continental shelf of the central Ross Sea. A 185-m-thick interval between 380 and 565 m is dominated by diamictite and records a time when marine-based ice sheets expanded across the continental shelf (*56*). This coincides with maximum eccentricity-precession variance at the apex of the 2.4-Myr grand cycle, which is also a time of high δ^{18}O S_{obl} (*39*). The 1.2-Myr obliquity grand cycles alternate between greater and lesser maxima of amplitude modulation (Figs. 2B and 3B). Our study interval at IODP U1521A coincides with the transition between one of these lesser maxima and a node, unlike AND-2A, which coincides with the maxima of the larger 1.2-Myr cycle (Figs. 2B and 3B).

RESULTS

Cyclostratigraphy of IODP U1521A

Sediment core U1521A was drilled in the Ross Sea as part of IODP Expedition 374 (*56*) (Fig. 1). The site is located at −75.683918°, −179.671847° in the Pennell Basin at a water depth of ~562 m (*56*) and comprises 650.1 m of strata, which include diatomaceous sediments, mudstone, occasional chert nodules, and diamictite (*57*). Geochronological constraints come from paleomagnetic reversals, and biostratigraphic data from diatoms and radiolarians (*57*). Geochemical and petrological information from this site has previously been used to reveal the early Miocene history of the WAIS and its expansion into the Ross Sea (*22*, *23*).

Astrochronological analyses are conducted on clast abundance data from IODP Site U1521A for the interval between 380 and 565 m, which is dominated by diamictite facies but includes thinner intervals

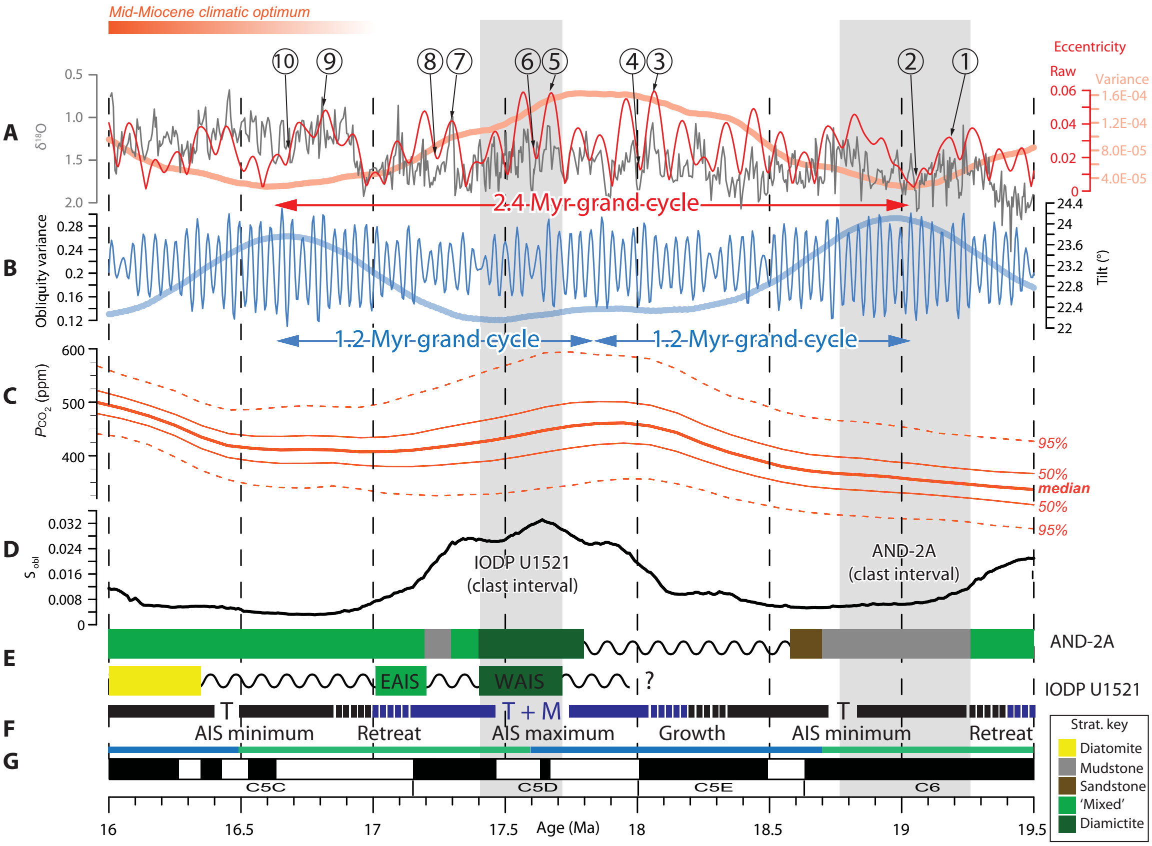

Fig. 3. A synthesis of proxy data, astronomical parameters, Ross Sea stratigraphy, and cryosphere behavior. (**A**) Eccentricity (thin red line), short eccentricity variance (thick orange line; 1-Myr moving window), and the $\delta^{18}O$ megasplice (*40*) based primarily on data from IODP site U1337 (*38*) (gray; with axis inverted). The numbers in white circles refer to the timing of numbered episodes referenced in Fig. 4. (**B**) Obliquity (thin blue line) and obliquity variance (thick blue line; 1-Myr moving window), showing the 1.2-Myr grand cycles (*41*). (**C**) Reconstruction of $P\text{CO}_2$ based on a compilation of proxy data (*16*). The thick line represents a 100-kyr median of community-vetted proxy data, while thinner lines represent 50% (solid) and 95% (dashed) credible intervals. (**D**) $\delta^{18}O$ obliquity sensitivity curve for a 1-Ma moving window (*39*). (**E**) Chronostratigraphy and facies for AND-2A (*29*, *63*, *102*) (top) and IODP U1521A (*22*, *56*) (bottom). "EAIS" and "WAIS" reflect interpreted sediment source based on provenance data (*22*). (**F**) Regional patterns of interpreted trends in ice sheet growth and configuration reflecting predominantly terrestrial ("T") or marine-terminating ("M") states. (*22*, *39*). (**G**) Geomagnetic polarity timescale (*66*).

of mudstone (*58*, *59*) (Figs. 2 and 3). Seismic profiles show that this interval consists of thick progradational wedges and, when integrated with the sedimentological, provenance, and age model data, indicates near continuous accumulation in a glacimarine depositional environment proximal to the margin of a marine-based WAIS (*23*, *56*). Geochronological constraints from diatoms and magnetic polarity reversals suggest an age between 17.4 and 17.8 Ma, with plausible depositional rates between ~30 and ~65 cm/kyr (*22*, *56*).

Astrochronologic evaluation of the clast abundance data via the TimeOpt method (*60*, *61*) identifies an optimal sedimentation rate of 60.12 cm/kyr that is highly significant ($r^2_{\text{opt}} = 0.399$; $P = 0.005$), based on 2000 Monte Carlo simulations using power law surrogates (see Materials and Methods and Supplementary Text). Using this calibration, the largest spectral power peak aligns with the main obliquity cycle (40.3 kyr), a subsidiary peak aligns with the 53-kyr obliquity solution term, and additional large peaks align with long and short eccentricity (Fig. 2D, top panel), although the short duration of the study interval (~308 kyr) is only marginally suitable for robust quantification of these lower frequency cycles. Very little spectral power is concentrated in precession bandwidths, and there is a modest un-aligned power spectrum peak between obliquity and precession, with a period of 26.5 kyr, which is plausibly related to the weak 30-kyr obliquity cycle.

This "floating" astrochronology from IODP U1521A is anchored based on various independent sources of geochronological constraint (*22*, *56*) and by means of automated and manual tuning to an astronomical solution. Several manually tuned interpretations are discussed in Supplementary Text and provide a useful comparison between the stratigraphic data and expected astronomical forcing. The ages reported in Figs. 2 and 3 are derived from independent geochronology (*22*), including diatom occurrence data and paleomagnetic reversal stratigraphy. The automated anchoring method "slideCor" in the R package "astrochron" (*60*) finds an optimal match between an astronomical solution and a floating astrochronology. Independent biostratigraphic and magnetostratigraphic constraints restrict the slideCor analysis to a conservatively defined ~800-kyr interval between 17.154 Ma (based on the C5Cr/C5Dn MPR) and 17.950 Ma (based on the absence of *Thalassiosira praefraga* in biostratigraphic samples) (*22*). The slideCor analysis yields several plausible ages for anchoring the floating timescale. We have selected

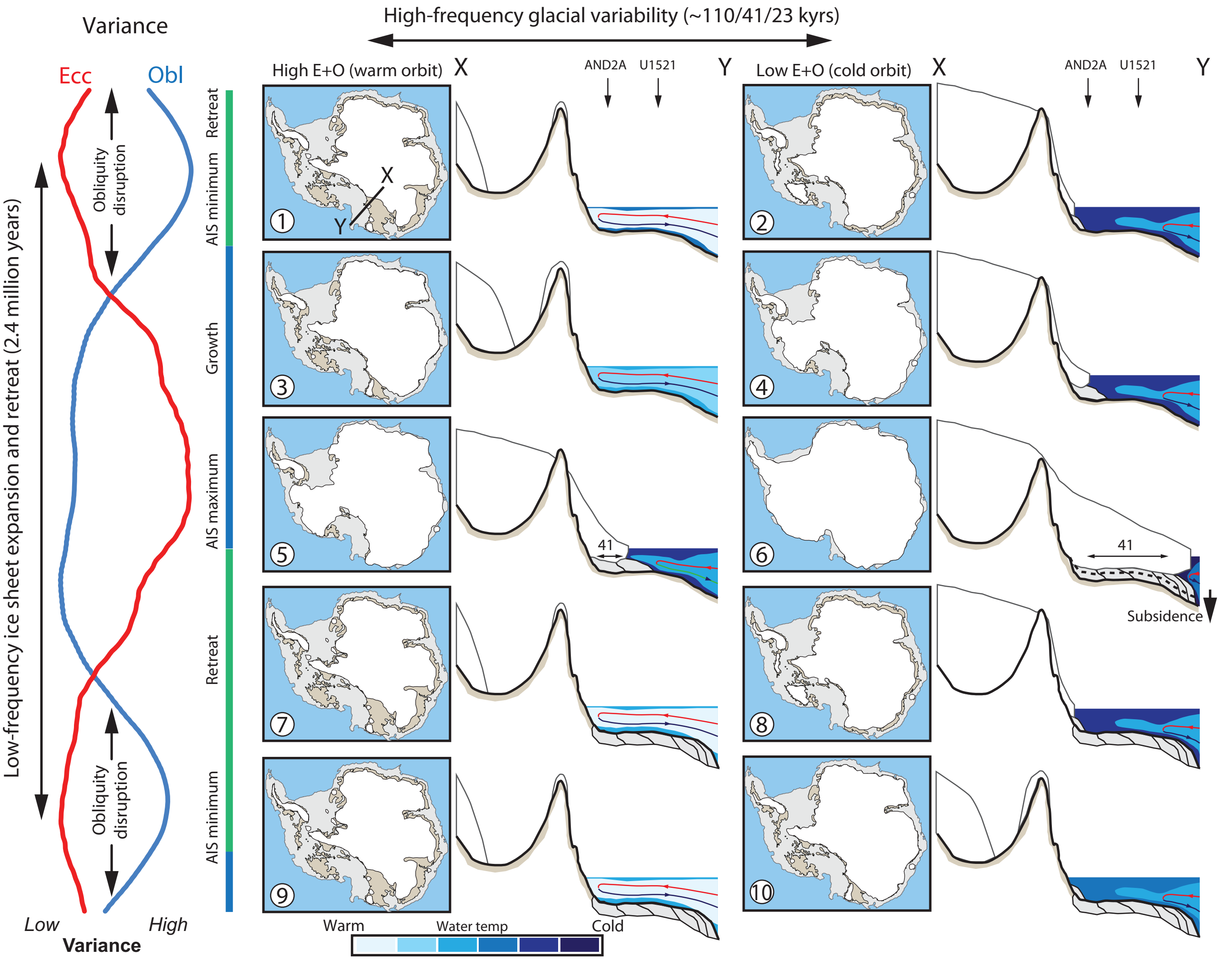

Fig. 4. Schematic diagrams summarizing key climatic and cryosphere shifts over an early Miocene "grand cycle." This shows changes in ice sheet configuration and oceanographic conditions across high-frequency 110- and 41-kyr (glacial to interglacial) episodes (left to right) and over a low-frequency grand cycle (top to bottom). The timing of episodes 1 to 10 is shown on the eccentricity curve in Fig. 3A. Curves from Fig. 3 (A and B) are transposed at the left of Fig. 4 to reflect long-term changes in astronomical forcing.

an anchor that results in an age range from 17.401 to 17.709 Ma and a slideCor r^2 value of 0.703. Although there are other anchors that yield a slightly higher r value in the ~800-kyr age range, the one selected here is most consistent with a paleomagnetic interpretation developed in earlier studies of this site (Fig. 3) (*22*).

Cyclostratigraphy of AND-2A

AND-2A was drilled at −77.758141°, 165.276765° in water ~384 m deep (*62*). A sedimentary sequence was recovered to 1138.54 m below seafloor, and is primarily diamictite, with distinct intervals of sand and fine-grained clastic mudstone (*29*, *63*). Astrochronological analyses are conducted on clast abundance data in AND-2A through the interval between 800 and 900 m, which comprises a relatively continuous interval of mud with few interbedded sands (*24*). Independent geochronological constraints from paleomagnetism (*64*, *65*), diatom biostratigraphy (*62*), and ^{40}Ar/^{39}Ar dates from pumice clasts (*39*, *54*) indicate that this interval ranges from ~18.6 to ~19.5 Ma (*24*), within the duration of magnetochron C6n (*65*, *66*). This suggests plausible depositional rates between 10 and 25 cm/kyr.

Astrochronologic evaluation of the clast abundance data (*67*) via the TimeOpt method identifies an optimal sedimentation rate of 20.76 cm/kyr that is highly significant ($r^2_{\mathrm{opt}} = 0.172$; $P = 0.005$ using an AR1 stochastic null model; see Materials and Methods and Supplementary Text). Using this temporal calibration, large power spectrum peaks align with long (405 kyr) and short (90 to 130 kyr) eccentricity, with additional large spectral peaks aligning with precession (19.0 and 20.2 kyr). A substantial power spectrum peak aligns with a weak long obliquity cycle (52.8 kyr), with a smaller peak close to the obliquity term that dominates the theoretical astronomical solution (40.3 kyr) (Fig. 2D, bottom panel).

As with IODP U1521A, a series of automated and manual tuning interpretations have been generated for AND-2A, using different cyclic components. The age range presented here (Figs. 2 and 3) is constrained by independent geochronology (*24*, *54*, *55*) and by automated anchoring of the floating astrochronology with the slideCor function (*60*), which suggests that the AND-2A section spans 18.772 to 19.253 Ma, with an r^2 of 0.417.

Counterintuitively, this suggests that our study interval of AND-2A records a robust signal of short eccentricity and precession during a time when the variance in external forcing for these parameters should be minimal (*41*) (Fig. 2A). This discrepancy is unlikely to be due to uncertainties in the astronomical solution, as prior modeling exercises conclude that the full eccentricity solution used here is valid to 40 Ma, an observation confirmed by the strong consistency of eccentricity solutions generated by independent studies over this time interval (*41*, *68*–*70*).

The observed ice sheet variability is more likely due to a dynamic and nonlinear cryosphere response to astronomical forcing. For example, work in the Plio-Pleistocene indicates a compelling anti-phase relationship between the variance of eccentricity forcing and the corresponding eccentricity variance recorded in benthic δ^{18}O (*71*, *72*). These studies argue that, during the past 5 Ma, internal feedbacks of the climate and cryosphere can result in strong eccentricity-scale ice sheet growth when precession (and eccentricity) is weak, as this condition allows the persistence of cool summertime conditions that would otherwise be disrupted every ~20 kyr (*71*–*75*). It is possible that the AIS behaved more like the Pleistocene Northern Hemisphere Ice Sheet under the temperate to subpolar climate conditions that characterized Antarctica during the Miocene (*19*, *76*). In any case, similar to the Plio-Pleistocene (*71*, *73*), our results suggest that a nonlinear process linked to the amplitude modulation of precession by eccentricity is important in generating ~100-kyr glacial cycles during specific ice sheet or climate states. In general, we refer to such variability as a signal of eccentricity, recognizing that this is a simplification of a complex system of internal feedbacks.

We also considered the possibility of errors in the age model and explored alternative TimeOpt interpretations, manual tuning approaches, and automated slideCor anchors for floating astrochronologies (see discussion in Supplementary Text). However, each viable age model presented here coincides with times where substantial obliquity forcing is predicted by theory (*41*) but is not observed in the AND-2A clast abundance dataset. Although only one age model is presented in the main body of this paper, all three are consistent with the conceptual framework elaborated in the following section.

DISCUSSION

Results from AND-2A (Fig. 2D, bottom plot) show strong signals of eccentricity and precession (with a subsidiary obliquity contribution) during the Early Miocene when Antarctica was covered by large, but predominantly terrestrial, ice sheets. This is consistent with astronomical forcing of the ice sheet by local summertime insolation (*77*), with the contribution of eccentricity-scale variability by internal feedbacks and nonlinear responses of climate and cryosphere, as discussed above (*71*–*73*).

By contrast, the clast record from IODP U1521A (Fig. 2D, top plot), deposited when ice had expanded widely across the continental shelf with a major marine-based advance of the WAIS margin, has comparatively more spectral power concentrated around the 41-kyr obliquity cycle. These observations tether the obliquity sensitivity results developed from distal δ^{18}O records by Levy *et al.* (*39*) to ice-proximal sections and proxy datasets that directly capture ice sheet response (Fig. 3).

We integrate the astrochronologically calibrated proximal records (Fig. 2) with a regional synthesis of stratigraphic observations through the Miocene (Fig. 3) (*19*, *22*, *24*, *39*, *78*). From this, we develop a model to explain how astronomically driven radiative variations and ocean-cryosphere interactions drive ice sheet variability during the Miocene over higher frequency cycles (~100, 41, and 23 kyr) and long-period "grand cycles" (~2.4 and 1.2 Myr), augmented by glacial sedimentary processes and isostatic adjustment (Fig. 4). Over multi-kyr intervals, precession, modulated by short-period eccentricity (~100 ka), plays a key role, which is clearly reflected in δ^{18}O records that indicate episodes of cold bottom water temperature and ice volume maxima (reflected by higher δ^{18}O values) that generally occur during intervals of low eccentricity (e.g., Figs. 3A and 4, episodes 2, 4, 6, and 8). Warmer bottom water temperature and ice volume minima occur during high eccentricity forcing (*28*, *79*) (e.g., Figs. 3A and 4, episodes 1, 3, 5, 7, and 9).

Over the course of the 2.4-Myr grand cycles, eccentricity variance changes substantially and approaches zero during "nodes," where it remains relatively low for a sustained interval (e.g., 18.8 to 19.2 Ma and 16.4 to 16.8 Ma; Fig. 3A). In contrast, obliquity forcing and its variance are substantial even during long-term 1.2-Myr nodes (*41*) (Fig. 3B). Theoretical obliquity and eccentricity/precession variance are anti-phased at the million-year scale, and the 1.2-Myr obliquity cycle has a 2.4-Myr modulation, where large 1.2-Myr maxima alternate with smaller maxima (see Fig. 3, A and B). Every ~2.4 Myr, the summertime insolation due to obliquity is the highest and equator-pole temperature gradient is the weakest, at which time loss of sea ice and enhanced upwelling of warm deep ocean water results in melting and retreat of the marine-terminating ice margin. These patterns are characterized in detail in (*39*), but see also (*45*, *80*).

We propose the label "obliquity disruption" for this mechanism, as consecutive intervals of high obliquity every ~2.4 Myr forces ice retreat related to meridional gradient-controlled oceanic heat delivery to marine-terminating margins, even when eccentricity and precession summertime forcing is minimized (e.g., ~19.1 Ma). The signature of obliquity disruption at the margin of the early Miocene Antarctic ice sheet is captured in the 100-m mud-rich interval of AND-2A, deposited between ~19.2 and ~18.7 Ma (Fig. 3E).

Regional data show that this phase of obliquity disruption ended at ~18.7 Ma when the AIS advanced well beyond the AND-2A site and grounded in marine environments across the Ross Sea continental shelf (*22*). This growth coincided with a gradual decline in the variance in local insolation forcing and strengthening of the Southern Hemisphere meridional temperature gradient that occurred as long-term obliquity-forcing variance decreased through successive glacial/interglacial cycles and interglacial periods became cooler (*19*, *24*) (Fig. 3, A and B). More frequent and consecutive episodes of near-zero eccentricity also reduced seasonal variability and the frequency of the warmest summers.

Sediment that was deposited as the AIS progressively advanced and retreated into the marine environment over subsequent high-frequency glacial cycles (*22*) likely caused the continental shelf to shoal. Progradational packages of sediment formed a platform across which the ice sheet advanced across the Ross Sea continental shelf over multi-kyr to multi-Myr timescales (Fig. 4, episodes 4 to 6). These packages of sediment are captured in Ross Sea Seismic units that often comprise prograding sequences up to 200 m in thickness (*23*, *78*). The sensitivity of the ice sheet to obliquity forcing (reflected by the S_{obl} of δ^{18}O; Fig. 3D) was amplified as the AIS advanced into marine environments and the area of ice in contact with the ocean increased. $\delta^{18}O$ S_{obl} peaked when the AIS reached maximum extent (*22*), which occurred during sustained low-obliquity forcing variance [~17.75 to ~17.4 Ma (*56*)]. This orbital configuration produced the coldest consecutive interglacial climate and allowed marine-based ice sheets to persist during successive interglacial episodes. A peak in near-field sea level due to an increase in the gravitational attraction of the ice sheet may have caused shoaling of the thermocline relative to the continental shelf. This likely enhanced interactions between warm deep water at the continental shelf margin and marine-based ice, amplifying the influence of smaller changes in obliquity (Fig. 4, episodes 5 and 6) and ultimately served to limit further advance of the AIS (Fig. 4, episode 6). These processes are captured in the interval deposited between ~17.7 and ~17.4 Ma at IODP site U1521A, which records strong obliquity in clast abundance data, despite the prediction that obliquity should be weak through this interval (Fig. 2).

An increase in interglacial summer temperatures occurred as the system transitioned to an interval of increased obliquity forcing variance and decreased eccentricity variance between 17.2 and 17 Ma. This transition started a new phase of increasing obliquity disruption and gradual marine ice sheet retreat over a ~1.2-Myr period. Environmental data in the Ross Sea drill cores indicate the AIS once again retreated from marine environments to and beyond the continent's terrestrial margins under these astronomical forcing conditions (*22*) (Figs. 3A and 4, episodes 7 and 8). Deepening of the continental shelf due to rapid glacial erosion on the inner shelf from preceding marine-based advances (*22*), sediment loading on the outer shelf (*81*), and thermal subsidence or tectonic rifting (*21*, *82*) allowed warm deep water to flow across the continental shelf once again and likely played a complementary role in driving the observed ice sheet retreat. Reduced ice volume and extent is reflected by an increase in ice distal facies in U1521A and a sharp decrease in $\delta^{18}O$ at the onset of the Miocene Climate Optimum (*38*) (~17 Ma; Fig. 3A). This episode of long-term AIS retreat yields a minimum in $\delta^{18}O$ S_{obl} and marks the "end" of a 2.4-Myr cycle of ice sheet expansion and contraction.

This work provides insights into the past and future of the Earth's largest ice sheets. Through a synthesis of geological data from the Ross Sea, we identify astronomically influenced cyclic variability at the margins of the AIS between terrestrial and marine-terminating states during the early Miocene. When combined with prior research (*39*), we conclude that marine-based portions of Antarctica's ice sheets were particularly sensitive to obliquity forcing during the late Oligocene to mid-Miocene, when proxies indicate that baseline atmospheric P_{CO_2} concentrations ranged between 400 and 600 ppm (Fig. 3) (*15*, *16*, *19*, *83*) and sea ice extent was limited. Today, Earth's obliquity forcing variance is near a 2.4-Myr maximum (*41*). Our interpretations suggest that these warm astronomical conditions can enhance ocean-driven melt at the ice sheet margin. Antarctica's continental shelves deepen inland, creating a dynamical instability that enhances marine–ice sheet retreat and ice volume loss (*84*, *85*). Collectively, these findings underscore the necessity of stabilizing or reducing atmospheric P_{CO_2} to prevent the AIS from returning to small terrestrial-based ice sheets that characterized much of the early to middle Miocene.

MATERIALS AND METHODS

Clast abundance data

Sediment clast abundance data have been published previously from IODP site U1521A (*22*) and from AND-2A (*24*, *86*, *87*). In both cases, clasts above 2 mm in diameter (gravel) were manually counted and individually classified along the cut surface of the archive half sections of the core, which were then binned into 10-cm core intervals. These methods adhere to the methodologies set out in the ANDRILL Project and Cape Roberts Project (CRP) programs (*88*–*91*). Both datasets are publicly available [see supplemental R code (data S1) for additional details].

Astrochronology: ETP

The theoretical astronomical solutions used for the analyses presented here derive from the work of Laskar *et al.* (*41*) using the function "etp" in the R package astrochron (*60*). The normalized eccentricity-tilt-precession (ETP) models are determined by summing the standardized parameters so that all astronomical components are equally weighted: Eccentricity, tilt, and precession are each adjusted to zero mean and unit variance (*92*).

Astrochronology: TimeOpt

Sediment clast abundance data have been analyzed using "TimeOpt" (*52*), which is a statistical optimization method for astronomical timescale construction and astrochronologic testing, executed by the astrochron package in R (*60*). Given a range of plausible depositional rate parameters and a series of specified astronomical periodicities (for precession, obliquity, and eccentricity), TimeOpt identifies the age model that results in a time series that best aligns with the predictions of Milankovitch theory. Specifically, two diagnostic attributes of the astronomical hypothesis are evaluated: the hierarchy of cyclic frequencies expected of Milankovitch cycles ($r^2_{spectral}$), and the match between eccentricity cycles and the envelope of precession amplitude modulation ($r^2_{envelope}$) (*61*, *93*). These two values are multiplied to produce an r^2_{opt} value, which provides insight into the strength of a hypothesized astronomical signal at each evaluated sedimentation rate.

Estimates for minimum and maximum plausible depositional rates are derived from independent geochronological, biostratigraphic, and magnetostratigraphic data. The target astronomical periods have been estimated from the theoretical astronomical solution (*41*), with dominant frequencies isolated using the multitaper method [MTM; (*60*, *94*, *95*)]. The key frequencies for our analyses are summarized in the Supplementary Materials (see data S1). Although the resulting astrochronologies are consistent with a manual tuning approach (described in the next section), the TimeOpt-derived interpretations require fewer "researcher degrees of freedom," and we therefore emphasize this approach. Since, by default, TimeOpt assumes a constant depositional rate, the astrochronologies presented here may not capture fine-scale variability in sedimentation. However, we argue that the approximation generated by this approach is sufficient to provide necessary insights into the nature of Milankovitch cyclicity at both sites.

Subsequently, a Monte Carlo astrochronologic test is conducted to evaluate the null hypothesis that the observed variability in clast abundance arises entirely by stochastic processes, rather than astronomical forcing. The Monte Carlo simulations are generated using the function "timeOptSim" or "timeOptSimPwrLaw," which creates many similar time series of stochastic ("red") noise, to assess the probability that such datasets can produce an r^2_{opt} value comparable to the one generated by the clast abundance data (*61*). This analysis yields a *P* value, indicating whether the null hypothesis (i.e., the data are generated from a stochastic "red noise" process) can be rejected with a high degree of confidence. An AR1 stochastic process provides the best fit to the spectral background in the AND-2A clast abundance data, while a power law process yields the best background fit for U1521A (see Supplementary Text and figures).

Astrochronology: Tuning and SlideCor

Astrochronological interpretations are often conducted by direct matching ("tuning") of cyclic components of a stratigraphic dataset to corresponding patterns observed in an astronomical solution or model (*96*). This is particularly valuable when developing astronomical timescales that are anchored to a numerical age (rather than floating timescales). In this present work, we compare two approaches for the development of anchored astronomical timescales: an automated quantitative method (i.e., the R functions TimeOpt and slideCor in package astrochron) and manual tuning.

For the primary age models used here (Fig. 2), we rely upon the automated tuning approach, which is constrained by published geochronological data for AND-2A and IODP U1521A. Specifically, the floating astronomical timescales derived by the TimeOpt analyses (using a constant sedimentation model) are anchored to theoretical solutions using the slideCor function in the R package astrochron (*60*). This approach seeks to anchor a floating astrochronology by finding the age that results in the largest r value (Pearson correlation coefficient). If the phase relationship between proxy value and astronomical forcing is not known precisely (as is the case here), r^2 provides a more conservative approach, allowing for positive and negative correlations to be considered.

We have applied slideCor using a specified cyclic component that has been filtered from the TimeOpt calibrated floating astrochronology. In each case, we have selected the cycle with the highest spectral power: short eccentricity in AND-2A and obliquity in IODP U1521A. These have been matched to the respective components of the astronomical solution, and r^2 values have been used to inform plausible anchoring age ranges for the studied intervals. Given the uncertainty in phase relationship between forcing and response, an uncertainty of ± half of the tuning period is assigned to the anchored astrochronologies.

For the supplemental manual tuning approach, we have isolated the cyclic components of eccentricity, obliquity, and precession from each stratigraphic dataset in the depth domain, using a bandpass filter (*97*). The spatial wavelengths of these spectral components are informed by the TimeOpt analyses that have been conducted. The filtered clast abundance time series representing eccentricity, obliquity, and precession are manually tuned, independently, to their corresponding astronomical components of the theoretical solution. This is done by visually matching cycles in stratigraphy, to plausibly equivalent cycles in the astronomical solution, guided by independent geochronological constraint (when available), and by changes in the amplitude modulation of the cyclic components.

The manual approach has been applied both for IODP U1521A and for AND-2A in this study. Although more subjective, this complimentary approach has some potential advantages, specifically: (i) It allows for variable sedimentation rates within the study interval, (ii) it is based on detailed visual comparison between stratigraphic data and the roughly co-eval parts of the astronomical solution, and (iii) each tuning option provides an independent test of narrowband components of a holistic astrochronological interpretation. For example, a dataset that has been calibrated to eccentricity will necessarily concentrate spectral power in eccentricity bandwidths. If, however, independently of this, spectral power is also concentrated in obliquity or precession bandwidths, this offers support of an astrochronological interpretation ("minimal tuning") (*98*). Results from these analyses are plotted and described in more detail in Supplementary Text.

Supplementary Materials

The PDF file includes:

Supplementary Text
Full list of IODP Expedition 374 Scientists
Figs. S1 to S23
Legend for data S1
References

Other Supplementary Material for this manuscript includes the following:

Data S1

REFERENCES AND NOTES

1. IPCC, *Climate Change 2021: The Physical Science Basis. Contribution of Working Group I to the Sixth Assessment Report of the Intergovernmental Panel on Climate Change* (IPCC, 2021).
2. M. E. Raymo, K. H. Nisancioglu, The 41 kyr world: Milankovitch's other unsolved mystery. *Paleoceanography* **18**, 1011 (2003).
3. R. M. DeConto, D. Pollard, P. A. Wilson, H. Pälike, C. H. Lear, M. Pagani, Thresholds for Cenozoic bipolar glaciation. *Nature* **455**, 652–656 (2008).
4. J. S. Crampton, R. D. Cody, R. Levy, D. Harwood, R. McKay, T. R. Naish, Southern Ocean phytoplankton turnover in response to stepwise Antarctic cooling over the past 15 million years. *Proc. Natl. Acad. Sci. U.S.A.* **113**, 6868–6873 (2016).
5. D. Pollard, R. M. DeConto, R. B. Alley, Potential Antarctic Ice Sheet retreat driven by hydrofracturing and ice cliff failure. *Earth Planet. Sci. Lett.* **412**, 112–121 (2015).
6. S. C. Woodard, Y. Rosenthal, K. G. Miller, J. D. Wright, B. K. Chiu, K. T. Lawrence, Antarctic role in Northern Hemisphere glaciation. *Science* **346**, 847–851 (2014).
7. B. de Boer, A. M. Dolan, J. Bernales, E. Gasson, H. Goelzer, N. R. Golledge, J. Sutter, P. Huybrechts, G. Lohmann, I. Rogozhina, A. Abe-Ouchi, F. Saito, R. S. W. van de Wal, Simulating the Antarctic ice sheet in the late-Pliocene warm period: PLISMIP-ANT, an ice-sheet model intercomparison project. *Cryosphere* **9**, 881–903 (2015).
8. J.-M. Barnola, D. Raynaud, Y. S. Korotkevich, C. Lorius, Vostok ice core provides 160,000-year record of atmospheric CO_2. *Nature* **329**, 408–414 (1987).
9. L. E. Lisiecki, M. E. Raymo, A Pliocene-Pleistocene stack of 57 globally distributed benthic $\delta^{18}O$ records. *Paleoceanography* **20**, PA1003 (2005).
10. M. R. Legrand, C. Lorius, N. I. Barkov, V. N. Petrov, Vostok (Antarctica) ice core: Atmospheric chemistry changes over the last climatic cycle (160,000 years). *Atmos. Environ.* **22**, 317–331 (1988).
11. T. Stocker, *Climate Change 2013: The Physical Science Basis: Working Group I Contribution to the Fifth Assessment Report of the Intergovernmental Panel on Climate Change* (Cambridge Univ. Press, 2014).
12. Y. You, M. Huber, R. Müller, C. Poulsen, J. Ribbe, Simulation of the middle Miocene climate optimum. *Geophys. Res. Lett.* **36**, L04702 (2009).
13. R. Greenop, G. L. Foster, P. A. Wilson, C. H. Lear, Middle Miocene climate instability associated with high-amplitude CO_2 variability. *Paleoceanography* **29**, 845–853 (2014).
14. M. Pagani, J. C. Zachos, K. H. Freeman, B. Tipple, S. Bohaty, Marked decline in atmospheric carbon dioxide concentrations during the Paleogene. *Science* **309**, 600–603 (2005).
15. Y. G. Zhang, M. Pagani, Z. Liu, S. M. Bohaty, R. DeConto, A 40-million-year history of atmospheric CO2. *Philos. Trans. R. Soc. A Math. Phys. Eng. Sci.* **371**, 20130096 (2013).
16. Cenozoic CO2 Proxy Integration Project (Cenco2PIP) Consortium, Toward a Cenozoic history of atmospheric CO_2. *Science* **382**, eadi5177 (2023).
17. M. Guillermic, S. Misra, R. Eagle, A. Tripati, Atmospheric CO_2 estimates for the Miocene to Pleistocene based on foraminiferal $\delta^{11}B$ at Ocean Drilling Program Sites 806 and 807 in the Western Equatorial Pacific. *Clim. Past* **18**, 183–207 (2022).
18. D. Liebrand, H. M. Beddow, L. J. Lourens, H. Pälike, I. Raffi, S. M. Bohaty, F. J. Hilgen, M. J. M. Saes, P. A. Wilson, A. E. van Dijk, D. A. Hodell, D. Kroon, C. E. Huck, S. J. Batenburg, Cyclostratigraphy and eccentricity tuning of the early Oligocene through early Miocene (30.1-17.1 Ma): Cibicides mundulus stable oxygen and carbon isotope records from Walvis Ridge Site 1264. *Earth Planet. Sci. Lett.* **450**, 392–405 (2016).
19. R. H. Levy, A. M. Dolan, C. Escutia, E. G. Gasson, R. M. McKay, T. Naish, M. O. Patterson, L. F. Pérez, A. E. Shevenell, T. van de Flierdt, Antarctic environmental change and ice sheet evolution through the Miocene to Pliocene—A perspective from the Ross Sea and George V to Wilkes Land Coasts, in *Antarctic Climate Evolution*, F. Florindo, M. J. Siegert, L. De Santis, T. R. Naish, Eds. (Elsevier, ed. 2, 2022), pp. 389–521.

20. D. A. Handwerger, R. D. Jarrard, Neogene changes in Southern Ocean sedimentation based on mass accumulation rates at four continental margins. *Paleoceanography* **18**, 1081 (2003).
21. G. J. G. Paxman, E. G. W. Gasson, S. S. R. Jamieson, M. J. Bentley, F. Ferraccioli, Long-term increase in Antarctic ice sheet vulnerability driven by bed topography evolution. *Geophys. Res. Lett.* **47**, e2020GL090003 (2020).
22. J. W. Marschalek, L. Zurli, F. Talarico, T. van de Flierdt, P. Vermeesch, A. Carter, F. Beny, V. Bout-Roumazeilles, F. Sangiorgi, S. Hemming, L. F. Peréz, F. Colleoni, J. Prebble, T. E. van Peer, M. Perotti, I. Browne, A. Shevenell, D. K. Kulhanek, R. Levy, D. Harwood, N. B. Sullivan, S. R. Meyers, E. Griffith, C.-D. Hillenbrand, E. Gasson, M. J. Siegert, K. Licht, B. Keisling, G. Kuhn, J. Dodd, C. Boshuis, L. De Santis, R. M. McKay, IODP Expedition 374, A large West Antarctic Ice Sheet explains early Neogene sea-level amplitude. *Nature* **600**, 450–455 (2021).
23. L. F. Pérez, L. De Santis, R. M. McKay, R. D. Larter, J. Ash, P. J. Bart, G. Böhm, G. Brancatelli, I. Browne, F. Colleoni, Early and middle Miocene ice sheet dynamics in the Ross Sea: Results from integrated core-log-seismic interpretation. *GSA Bull.* **123**, 348–370 (2021).
24. R. H. Levy, D. Harwood, F. Florindo, F. Sangiorgi, R. Tripati, H. von Eynatten, E. Gasson, G. Kuhn, A. Tripati, R. DeConto, Antarctic ice sheet sensitivity to atmospheric CO_2 variations in the early to mid-Miocene. *Proc. Natl. Acad. Sci. U.S.A.* **113**, 3453–3458 (2016).
25. M. Kominz, K. Miller, J. Browning, M. Katz, G. Mountain, Miocene relative sea level on the New Jersey shallow continental shelf and coastal plain derived from one-dimensional backstripping: A case for both eustasy and epeirogeny. *Geosphere* **12**, 1437–1456 (2016).
26. K. G. Miller, J. V. Browning, W. J. Schmelz, R. E. Kopp, G. S. Mountain, J. D. Wright, Cenozoic sea-level and cryospheric evolution from deep-sea geochemical and continental margin records. *Sci. Adv.* **6**, eaaz1346 (2020).
27. S. F. Pekar, R. M. DeConto, High-resolution ice-volume estimates for the early Miocene: Evidence for a dynamic ice sheet in Antarctica. *Palaeogeogr. Palaeoclimatol. Palaeoecol.* **231**, 101–109 (2006).
28. D. Liebrand, A. T. M. de Bakker, H. M. Beddow, P. A. Wilson, S. M. Bohaty, G. Ruessink, H. Pälike, S. J. Batenburg, F. J. Hilgen, D. A. Hodell, C. E. Huck, D. Kroon, I. Raffi, M. J. M. Saes, A. E. van Dijk, L. J. Lourens, Evolution of the early Antarctic ice ages. *Proc. Natl. Acad. Sci. U.S.A.* **114**, 3867–3872 (2017).
29. C. R. Fielding, G. H. Browne, B. Field, F. Florindo, D. M. Harwood, L. A. Krissek, R. H. Levy, K. S. Panter, S. Passchier, S. F. Pekar, Sequence stratigraphy of the ANDRILL AND-2A drillcore, Antarctica: A long-term, ice-proximal record of Early to Mid-Miocene climate, sea-level and glacial dynamism. *Palaeogeogr. Palaeoclimatol. Palaeoecol.* **305**, 337–351 (2011).
30. T. R. Naish, K. J. Woolfe, P. J. Barrett, G. S. Wilson, C. Atkins, S. M. Bohaty, C. J. Bücker, M. Claps, F. J. Davey, G. B. Dunbar, A. G. Dunn, C. R. Fielding, F. Florindo, M. J. Hannah, D. M. Harwood, S. A. Henrys, L. A. Krissek, M. Lavelle, J. van der Meer, W. C. McIntosh, F. Niessen, S. Passchier, R. D. Powell, A. P. Roberts, L. Sagnotti, R. P. Scherer, C. P. Strong, F. Talarico, K. L. Verosub, G. Villa, D. K. Watkins, P. N. Webb, T. Wonik, Orbitally induced oscillations in the East Antarctic ice sheet at the Oligocene/Miocene boundary. *Nature* **413**, 719–723 (2001).
31. S. P. Gulick, A. E. Shevenell, A. Montelli, R. Fernandez, C. Smith, S. Warny, S. M. Bohaty, C. Sjunneskog, A. Leventer, B. Frederick, Initiation and long-term instability of the East Antarctic Ice Sheet. *Nature* **552**, 225–229 (2017).
32. T. Williams, D. Handwerger, A high-resolution record of early Miocene Antarctic glacial history from ODP Site 1165, Prydz Bay. *Paleoceanography* **20**, PA2017 (2005).
33. E. Gasson, R. M. DeConto, D. Pollard, R. H. Levy, Dynamic Antarctic ice sheet during the early to mid-Miocene. *Proc. Natl. Acad. Sci. U.S.A.* **113**, 3459–3464 (2016).
34. A. R. W. Halberstadt, H. Chorley, R. H. Levy, T. Naish, R. M. DeConto, E. Gasson, D. E. Kowalewski, CO_2 and tectonic controls on Antarctic climate and ice-sheet evolution in the mid-Miocene. *Earth Planet. Sci. Lett.* **564**, 116908 (2021).
35. L. B. Stap, J. Sutter, G. Knorr, M. Stärz, G. Lohmann, Transient variability of the Miocene Antarctic ice sheet smaller than equilibrium differences. *Geophys. Res. Lett.* **46**, 4288–4298 (2019).
36. H. Palike, J. Frazier, J. C. Zachos, Extended orbitally forced palaeoclimatic records from the equatorial Atlantic Ceara Rise. *Quat. Sci. Rev.* **25**, 3138–3149 (2006).
37. K. Billups, H. Pälike, J. E. T. Channell, J. C. Zachos, N. J. Shackleton, Astronomic calibration of the late Oligocene through early Miocene geomagnetic polarity time scale. *Earth Planet. Sci. Lett.* **224**, 33–44 (2004).
38. A. Holbourn, W. Kuhnt, K. G. D. Kochhann, N. Andersen, K. J. Sebastian Meier, Global perturbation of the carbon cycle at the onset of the Miocene Climatic Optimum. *Geology* **43**, 123–126 (2015).
39. R. H. Levy, S. R. Meyers, T. R. Naish, N. R. Golledge, R. M. McKay, J. S. Crampton, R. M. DeConto, L. De Santis, F. Florindo, E. G. W. Gasson, D. M. Harwood, B. P. Luyendyk, R. D. Powell, C. Clowes, D. K. Kulhanek, Antarctic ice-sheet sensitivity to obliquity forcing enhanced through ocean connections. *Nat. Geosci.* **12**, 132–137 (2019).
40. D. De Vleeschouwer, M. Vahlenkamp, M. Crucifix, H. Pälike, Alternating Southern and Northern Hemisphere climate response to astronomical forcing during the past 35 m.y. *Geology* **45**, 375–378 (2017).
41. J. Laskar, P. Robutel, F. Joutel, M. Gastineau, A. C. M. Correia, B. Levrard, A long-term numerical solution for the insolation quantities of the Earth. *Astron. Astrophys.* **428**, 261–285 (2004).
42. M. M. Milankovitch, Kanon der Erdbestrahlung und sein Andwendung auf das Eiszeitenproblem. *R. Serbian Acad. Spec. Publ.* **33**, (1941).
43. A. Berger, Long-term variations of caloric insolation resulting from the Earth's orbital elements. *Quatern. Res.* **9**, 139–167 (1978).
44. P. Huybers, Early Pleistocene glacial cycles and the integrated summer insolation forcing. *Science* **313**, 508–511 (2006).
45. T. Naish, R. Powell, R. Levy, G. Wilson, R. Scherer, F. Talarico, L. Krissek, F. Niessen, M. Pompilio, T. Wilson, L. Carter, R. M. DeConto, P. Huybers, R. McKay, D. Pollard, J. Ross, D. Winter, P. Barrett, G. Browne, R. Cody, E. Cowan, J. Crampton, G. Dunbar, N. Dunbar, F. Florindo, C. Gebhardt, I. Graham, M. Hannah, D. Hansaraj, D. Harwood, D. Helling, S. Henrys, L. Hinnov, G. Kuhn, P. Kyle, A. Laufer, P. Maffioli, D. Magens, K. Mandernack, W. MacIntosh, C. Millan, R. Morin, C. Ohneiser, T. Paulsen, D. Persico, I. Raine, J. Reed, C. Riesselman, L. Sagnotti, D. Schmitt, C. Sjunneskog, P. Strong, M. Taviani, S. Vogel, T. Wilch, T. Williams, Obliquity-paced Pliocene West Antarctic ice sheet oscillations. *Nature* **458**, 322–328 (2009).
46. L. E. Lisiecki, M. E. Raymo, W. B. Curry, Atlantic overturning responses to Late Pleistocene climate forcings. *Nature* **456**, 85–88 (2008).
47. A. Timmermann, T. Friedrich, O. E. Timm, M. O. Chikamoto, A. Abe-Ouchi, A. Ganopolski, Modeling obliquity and CO2 effects on Southern Hemisphere climate during the past 408 ka. *J. Climate* **27**, 1863–1875 (2014).
48. P. Huybers, E. Tziperman, Integrated summer insolation forcing and 40,000-year glacial cycles: The perspective from an ice-sheet/energy-balance model. *Paleoceanography* **23**, PA1208 (2008).
49. J. R. Toggweiler, J. Russell, Ocean circulation in a warming climate. *Nature* **451**, 286–288 (2008).
50. H. Heinrich, Origin and consequences of cyclic ice rafting in the northeast Atlantic Ocean during the past 130,000 years. *Quatern. Res.* **29**, 142–152 (1988).
51. R. McKay, G. Browne, L. Carter, E. Cowan, G. Dunbar, L. Krissek, T. Naish, R. Powell, J. Reed, F. Talarico, T. Wilch, The stratigraphic signature of the late Cenozoic Antarctic Ice Sheets in the Ross Embayment. *Geol. Soc. Am. Bull.* **121**, 1537–1561 (2009).
52. S. R. Meyers, The evaluation of eccentricity-related amplitude modulation and bundling in paleoclimate data: An inverse approach for astrochronologic testing and time scale optimization. *Paleoceanography* **30**, 1625–1640 (2015).
53. L. A. Hinnov, New perspectives on orbitally forced stratigraphy. *Annu. Rev. Earth Planet. Sci.* **28**, 419–475 (2000).
54. G. Di Vincenzo, L. Bracciali, P. Del Carlo, K. Panter, S. Rocchi, ^{40}Ar–^{39}Ar dating of volcanogenic products from the AND-2A core (ANDRILL Southern McMurdo Sound Project, Antarctica): Correlations with the Erebus Volcanic Province and implications for the age model of the core. *Bull. Volcanol.* **72**, 487–505 (2010).
55. G. D. Acton, F. Florindo, L. Jovane, C. Ohneiser, L. Sagnotti, E. Strada, K. L. Verosub, G. S. Wilson, ANDRILL-SMS Science Team, Paleomagnetism of the AND-2A Core, ANDRILL Southern McMurdo Sound Project, Antarctica. *Terra Antarctica* **15**, 193–210 (2008).
56. R. M. McKay, L. De Santis, D. K. Kulhanek, J. A. Ash, F. Beny, I. B. Browne, G. Cortese, I. M. C. De Sousa, J. D. Dodd, O. E. Esper, J. G. Gales, D. H. Harwood, S. Ishino, B. K. Keisling, S. Kim, S. Kim, J. S. Laberg, R. M. Leckie, J. Müller, M. P. Patterson, B. R. Romans, O. R. Romero, F. Sangiorgi, O. Seki, J. P. Powell, A. Shevenell, S. S. Singh, S. Sugisaki, T. Van De Flierdt, T. E. Van Peer, W. Xiao, Z. Xiong, "Site U1521" in *International Ocean Discovery Program Expedition 374 Preliminary Report: Ross Sea West Antarctic Ice Sheet History: Ocean-Ice Sheet Interactions and West Antarctic Ice Sheet Vulnerability: Clues from the Neogene and Quaternary Record of the Outer Ross Sea Continental Margin*, R. M. McKay, L. De Santis, D. K. Kulhanek, Eds. (International Ocean Discovery Program, 2018), vol. 374.
57. R. M. McKay, L. De Santis, D. K. Kulhanek, J. L. Ash, F. Beny, I. M. Browne, G. Cortese, I. M. Cordeiro de Sousa, J. P. Dodd, O. M. Esper, J. A. Gales, D. M. Harwood, S. Ishino, B. A. Keisling, S. Kim, J. S. Laberg, R. M. Leckie, J. Müller, M. O. Patterson, B. W. Romans, O. E. Romero, F. Sangiorgi, O. Seki, A. E. Shevenell, S. M. Singh, S. T. Sugisaki, T. van de Flierdt, T. E. van Peer, W. Xiao, Z. Xiong, "Expedition 374 summary" in *Proceedings of the International Ocean Discovery Program 374*, R. M. McKay, L. De Santis, D. K. Kulhanek, Expedition 374 Scientists, Eds. (International Ocean Discovery Program, 2019).
58. R. M. McKay, L. De Santis, D. K. Kulhanek, Expedition 318 Scientists, Ross Sea West Antarctic ice sheet history. *Proc. Int. Ocean Discov. Prog.* **374**, 1–10 (2019).
59. L. Zurli, M. Perotti, F. Talarico, "Data report: Petrology of gravel-sized clasts from Site U1521 core, IODP Expedition 374, Ross Sea" in *Proceedings of the International Ocean Discovery Program, 374*, R. M. McKay, L. De Santis, D. K. Kulhanek, E. Scientists, Eds. (International Ocean Drilling Program, 2021).
60. S. R. Meyers, Package 'astrochron'—A computational tool for astrochronology (2014). 10.32614/CRAN.package.astrochron.
61. S. R. Meyers, Cyclostratigraphy and the problem of astrochronologic testing. *Earth Sci. Rev.* **190**, 190–223 (2019).

62. G. D. Acton, J. Crampton, G. Di Vincenzo, C. R. Fielding, F. Florindo, M. Hannah, D. Harwood, S. Ishman, K. Johnson, L. Jovane, ANDRILL-SMS Science Team, Preliminary integrated chronostratigraphy of the AND-2A core, ANDRILL Southern McMurdo Sound project, Antarctica. *Terra Antarctica* **15**, 211–220 (2008).
63. C. R. Fielding, C. Atkins, K. Bassett, G. Browne, G. Dunbar, B. Field, T. D. Frank, L. Krissek, K. Panter, S. Passchier, S. F. Pekar, S. Sandroni, F. Talarico, ANDRILL-SMS Science Team, "Sedimentology and stratigraphy of the AND-2A core, ANDRILL Southern McMurdo Sound project, Antarctica" in *Studies from the ANDRILL, Southern McMurdo Sound Project, Antarctica*, D. M. Harwood, F. Florindo, F. Talarico, R. H. Levy, Eds. (Terra Antarctica, 2008), vol. 15, pp. 77–112.
64. D. M. Harwood, F. Florindo, F. Talarico, R. H. Levy, Studies from the ANDRILL Southern McMurdo Sound Project, Antarctica. *Terra Antarctica* **15**, 235 (2008).
65. L. Jovane, F. Florindo, G. Acton, C. Ohneiser, L. Sagnotti, E. Strada, K. L. Verosub, G. S. WIlson, F. Iacoviello, R. H. Levy, S. Passchier, Miocene glacial dynamics recorded by variations in magnetic properties in the ANDRILL 2A Drill Core. *J. Geophys. Res. Solid Earth* **124**, 2297–2312 (2019).
66. J. Ogg, Geomagnetic polarity time scale, in *Geologic Time Scale 2020*, F. M. Gradstein, J. G. Ogg, M. Schmitz, G. Ogg, Eds. (Elsevier, 2020), pp. 159–192.
67. SMS Science Team, Total clast numbers per 10 cm in sediment core AND-2A [dataset]. PANGAEA (2010).
68. J. Laskar, M. Gastineau, J.-B. Delisle, A. Farrés, A. Fienga, Strong chaos induced by close encounters with Ceres and Vesta. *Astron. Astrophys.* **532**, L4 (2011).
69. J. Laskar, A. Fienga, M. Gastineau, H. Manche, La2010: A new orbital solution for the long-term motion of the Earth. *Astron. Astrophys.* **532**, A89 (2011).
70. R. E. Zeebe, Numerical solutions for the orbital motion of the solar system over the past 100 Myr: Limits and new results. *Astron. J.* **154**, 193 (2017).
71. L. E. Lisiecki, Links between eccentricity forcing and the 100,000-year glacial cycle. *Nat. Geosci.* **3**, 349–352 (2010).
72. S. R. Meyers, L. A. Hinnov, Northern Hemisphere glaciation and the evolution of Plio-Pleistocene climate noise. *Paleoceanography* **25**, PA3207 (2010).
73. A. Abe-Ouchi, F. Saito, K. Kawamura, M. E. Raymo, J. Okuno, K. Takahashi, H. Blatter, Insolation-driven 100,000-year glacial cycles and hysteresis of ice-sheet volume. *Nature* **500**, 190–193 (2013).
74. M. Raymo, The timing of major climate terminations. *Paleoceanography* **12**, 577–585 (1997).
75. B. Hobart, L. E. Lisiecki, D. Rand, T. Lee, C. E. Lawrence, Late Pleistocene 100-kyr glacial cycles paced by precession forcing of summer insolation. *Nat. Geosci.* **16**, 717–722 (2023).
76. A. R. Lewis, A. C. Ashworth, An early to middle Miocene record of ice-sheet and landscape evolution from the Friis Hills, Antarctica. *GSA Bull.* **128**, 719–738 (2016).
77. M. Milankovitch, Mathematische Klimalehre und astronomische Theorie der Klimaschwankungen. *Handbuch Klimatol.* **1**, (1930).
78. R. McKay, J. Cockrell, A. Shevenell, J. Laberg, J. Burns, M. Patterson, S. Kim, T. Naish, D. Harwood, R. Levy, J. Marschalek, T. van de Flierdt, S. Ishino, B. Keisling, I. Cordeiro de Sousa, G. Cortese, F. Sangiorgi, M. Leckie, J. Dodd, B. Duncan, L. Pérez, B. Romans, S. Kim, S. Bombard, I. Browne, T. van Peer, O. Seki, F. Colleoni, D. Kulhanek, L. De Santis, IODP Expedition 374 Science Team, Miocene ice sheet dynamics and sediment deposition in the Central Ross Sea, Antartica. *Geol. Soc. Am. Bull.* 10.1130/B37613.37611 (2024).
79. D. Liebrand, L. Lourens, D. Hodell, B. de Boer, R. Van de Wal, H. Pälike, Antarctic ice sheet and oceanographic response to eccentricity forcing during the early Miocene. *Clim. Past* **7**, 869–880 (2011).
80. H. Pritchard, S. R. Ligtenberg, H. A. Fricker, D. G. Vaughan, M. R. van den Broeke, L. Padman, Antarctic ice-sheet loss driven by basal melting of ice shelves. *Nature* **484**, 502–505 (2012).
81. F. Colleoni, L. De Santis, E. Montoli, E. Olivo, C. C. Sorlien, P. J. Bart, E. G. Gasson, A. Bergamasco, C. Sauli, N. Wardell, S. Prato, Past continental shelf evolution increased Antarctic ice sheet sensitivity to climatic conditions. *Sci. Rep.* **8**, 11323 (2018).
82. G. J. Paxman, S. S. Jamieson, F. Ferraccioli, M. J. Bentley, N. Ross, A. B. Watts, G. Leitchenkov, E. Armadillo, D. A. Young, The role of lithospheric flexure in the landscape evolution of the Wilkes Subglacial Basin and Transantarctic Mountains, East Antarctica. *J. Geophys. Res. Earth* **124**, 812–829 (2019).
83. J. R. Super, E. Thomas, M. Pagani, M. Huber, C. O'Brien, P. M. Hull, North Atlantic temperature and pCO_2 coupling in the early-middle Miocene. *Geology* **46**, 519–522 (2018).
84. C. Schoof, Ice sheet grounding line dynamics: Steady states, stability, and hysteresis. *J. Geophys. Res. Earth* **112**, F03S28 (2007).
85. R. H. Thomas, C. R. Bentley, A model for Holocene retreat of the West Antarctic ice sheet. *Quatern. Res.* **10**, 150–170 (1978).
86. F. M. Talarico, S. Sandroni, Early Miocene basement clasts in ANDRILL AND-2A core and their implications for paleoenvironmental changes in the McMurdo Sound region (western Ross Sea, Antarctica). *Global Planet. Change* **78**, 23–35 (2011).
87. K. Panter, F. Talarico, K. Bassett, P. Del Carlo, B. Field, T. Frank, S. Hoffmann, G. Kuhn, L. Reichelt, S. Sandroni, Petrologic and geochemical composition of the AND-2A core, ANDRILL Southern McMurdo Sound Project, Antarctica. *Terra Antartica* **15**, 147–192 (2009).
88. S. Sandroni, F. Talarico, Petrography and provenance of basement clasts and clast variability in CRP-3 drillcore (Victoria Land Basin, Antarctica). *Terra Antartica* **8**, 449–468 (2001).
89. F. Talarico, S. Sandroni, Petrography, mineral chemistry and provenance of basement clasts in the CRP-1 drillcore (Victoria Land Basin, Antarctica). *Terra Antartica* **5**, 601–610 (1998).
90. F. Talarico, S. Sandroni, C. R. Fielding, C. Atkins, Variability, petrography and provenance of basement clasts in core from CRP-2/2A, Victoria Land Basin, Antarctica. *Terra Antarctica* **7**, 529–544 (2000).
91. F. M. Talarico, S. Sandroni, Provenance signatures of the Antarctic Ice Sheets in the Ross Embayment during the Late Miocene to Early Pliocene: The ANDRILL AND-1B core record. *Global Planet. Change* **69**, 103–123 (2009).
92. J. Imbrie, J. D. Hays, D. G. Martinson, A. McIntyre, A. C. Mix, J. J. Morley, N. G. Pisias, W. L. Prell, N. J. Shackleton, The orbital theory of Pleistocene climate: Support from a revised chronology of the marine $\delta^{18}O$ record, in *Milankovitch and Climate: Understanding the Response to Orbital Forcing*, A. Berger, J. Imbrie, J. Hays, G. Kukla, Eds. (D. Reidel Pub. Company, 1984), pp. 269–305.
93. S. R. Meyers, A. Malinverno, Proterozoic Milankovitch cycles and the history of the solar system. *Proc. Natl. Acad. Sci. U.S.A.* **115**, 6363–6368 (2018).
94. S. R. Meyers, Seeing red in cyclic stratigraphy: Spectral noise estimation for astrochronology. *Paleoceanogr. Paleoclimatol.* **27**, PA3228 (2012).
95. D. J. Thomson, Spectrum estimation and harmonic analysis. *Proc. IEEE* **70**, 1055–1096 (1982).
96. F. J. Hilgen, W. Krijgsman, C. Langereis, L. Lourens, A. Santarelli, W. Zachariasse, Extending the astronomical (polarity) time scale into the Miocene. *Earth Planet. Sci. Lett.* **136**, 495–510 (1995).
97. M. T. Taner, "Attributes revisited" in *Technical Report* (Rock Solid Images Inc., 1992).
98. R. A. Muller, G. J. MacDonald, *Ice Ages and Astronomical Causes: Data, Spectral Analysis and Mechanisms* (Springer Science & Business Media, 2002).
99. K. Matsuoka, A. Skoglund, G. Roth, S. Tronstad, Y. Melvær, Quantarctica. *Norwegian Polar Inst.* **10**, (2018).
100. B. Dorschel, L. Hehemann, S. Viquerat, F. Warnke, S. Dreutter, Y. Schulze Tenberge, D. Accettella, L. An, F. Barrios, E. A. Bazhenova, J. Black, F. Bohoyo, C. Davey, L. de Santis, C. Escutia Dotti, A. C. Frémand, P. T. Fretwell, J. A. Gales, J. Gao, L. Gasperini, J. S. Greenbaum, J. Henderson Jencks, K. A. Hogan, J. K. Hong, M. Jakobsson, L. Jensen, J. Kool, S. Larin, R. D. Larter, G. L. Leitchenkov, B. Loubrieu, K. Mackay, L. Mayer, R. Millan, M. Morlighem, F. Navidad, F. O. Nitsche, Y. Nogi, C. Pertuisot, A. L. Post, H. D. Pritchard, A. Purser, M. Rebesco, E. Rignot, J. L. Roberts, M. Rovere, I. Ryzhov, C. Sauli, T. Schmitt, A. Silvano, J. E. Smith, H. Snaith, A. J. Tate, K. Tinto, P. Vandenbossche, P. Weatherall, P. Wintersteller, C. Yang, T. Zhang, J. E. Arndt. PANGAEA (2022).
101. S. R. Meyers, B. B. Sageman, L. A. Hinnov, Integrated quantitative stratigraphy of the Cenomanian-Turonian Bridge Creek Limestone Member using evolutive harmonic analysis and stratigraphic modeling. *J. Sediment. Res.* **71**, 628–644 (2001).
102. B. D. Field, G. H. Browne, C. R. Fielding, F. Florindo, D. M. Harwood, S. A. Judge, L. A. Krissek, K. S. Panter, S. Passchier, S. F. Pekar, S. Sandroni, F. M. Talarico, A sedimentological record of early Miocene ice advance and retreat, AND-2A drill hole, McMurdo Sound, Antarctica. *Geosphere* **14**, 1780–1803 (2018).
103. T. Naish, R. Powell, R. Levy, Background to the ANDRILL McMurdo Ice Shelf Project (Antarctica) and initial science volume. *Terra Antarctica* **14**, 121–130 (2007).
104. S. Passchier, G. Browne, B. Field, C. R. Fielding, L. A. Krissek, K. Panter, S. F. Pekar, ANDRILL-SMS Science Team, Early and middle Miocene Antarctic glacial history from the sedimentary facies distribution in the AND-2A drill hole, Ross Sea, Antarctica. *Geol. Soc. Am. Bull.* **123**, 2352–2365 (2011).
105. F. Florindo, R. K. Farmer, D. M. Harwood, R. D. Cody, R. Levy, S. M. Bohaty, L. Carter, A. Winkler, Paleomagnetism and biostratigraphy of sediments from Southern Ocean ODP Site 744 (southern Kerguelen Plateau): Implications for early-to-middle Miocene climate in Antarctica. *Global Planet. Change* **110**, 434–454 (2013).
106. M. Zattin, B. Andreucci, S. N. Thomson, P. W. Reiners, F. M. Talarico, New constraints on the provenance of the ANDRILL AND-2A succession (western Ross Sea, Antarctica) from apatite triple dating. *Geochem. Geophys. Geosyst.* **13**, Q10016 (2012).
107. M. Zattin, F. M. Talarico, S. Sandroni, Integrated provenance and detrital thermochronology studies on the ANDRILL AND-2A drill core: Late Oligocene–Early Miocene exhumation of the Transantarctic Mountains (southern Victoria Land, Antarctica). *Terra Nova* **22**, 361–368 (2010).
108. G. Wilson, R. Levy, G. Acton, T. Naish, D. Harwood, F. Florindo, R. Powell, Dating Antarctic climatic and tectonic events of the Neogene-Age models from the ANDRILL 1B and 2A cores. *AGU Fall Meet. Abstr.* **2008**, C21B-0542 (2008).
109. C. R. Fielding, J. Whittaker, S. A. Henrys, T. J. Wilson, T. R. Naish, Seismic facies and stratigraphy of the Cenozoic succession in McMurdo Sound, Antarctica: Implications for

tectonic, climatic and glacial history. *Palaeogeogr. Palaeoclimatol. Palaeoecol.* **260**, 8–29 (2008).

110. R. Nyland, K. Panter, S. Rocchi, G. Di Vincenzo, P. Del Carlo, M. Tiepolo, B. Field, P. Gorsevski, Volcanic activity and its link to glaciation cycles: Single-grain age and geochemistry of Early to Middle Miocene volcanic glass from ANDRILL AND-2A core, Antarctica. *J. Volcanol. Geotherm. Res.* **250**, 106–128 (2013).
111. M. P. S. Badger, C. H. Lear, R. D. Pancost, G. L. Foster, T. R. Bailey, M. J. Leng, H. A. Abeis, CO_2 drawdown following the middle Miocene expansion of the Antarctic Ice Sheet. *Paleoceanography* **28**, 42–53 (2013).
112. M. O. Patterson, S. E. Ishman, Neogene benthic foraminiferal assemblages and paleoenvironmental record for McMurdo Sound, Antarctica. *Geosphere* **8**, 1331–1341 (2012).
113. A. G. Beu, M. Taviani, Early Miocene Mollusca from McMurdo Sound, Antarctica (ANDRILL 2A drill core), with a review of Antarctic Oligocene and Neogene Pectinidae (Bivalvia). *Palaeontology* **57**, 299–342 (2014).
114. M. C. Marcano, S. Mukasa, K. C. Lohmann, C. Stefano, M. Taviani, A. Andronikov, Chronostratigraphic and paleoenvironmental constraints derived from the ^{87}Sr/^{86}Sr and δ^{18}O signal of Miocene bivalves, Southern McMurdo Sound, Antarctica. *Glob. Planet. Change* **69**, 124–132 (2009).
115. M. Taviani, M. Hannah, D. Harwood, S. Ishman, K. Johnson, M. Olney, C. Riesselman, E. Tuzzi, A. Beu, S. Blair, Palaeontological characterisation and analysis of the AND-2A core, ANDRILL Southern McMurdo Sound Project, Antarctica. *Terra Antartica* **15**, 113–146 (2008).
116. M. Baddouh, S. R. Meyers, A. R. Carroll, B. L. Beard, C. M. Johnson, Lacustrine ^{87}Sr/^{86}Sr as a tracer to reconstruct Milankovitch forcing of the Eocene hydrologic cycle. *Earth Planet. Sci. Lett.* **448**, 62–68 (2016).
117. N. B. Sullivan, S. R. Meyers, R. H. Levy, R. M. McKay, N. R. Golledge, G. Cortese, Millennial-scale variability of the Antarctic Ice Sheet during the Early Miocene. *Proc. Natl. Acad. Sci. U.S.A.* **120**, e2304152120 (2023).
118. L. E. Lisiecki, M. E. Raymo, Plio–Pleistocene climate evolution: Trends and transitions in glacial cycle dynamics. *Quat. Sci. Rev.* **26**, 56–69 (2007).
119. J. Zachos, M. Pagani, L. Sloan, E. Thomas, K. Billups, Trends, rhythms, and aberrations in global climate 65 Ma to present. *Science* **292**, 686–693 (2001).
120. T. Westerhold, N. Marwan, A. J. Drury, D. Liebrand, C. Agnini, E. Anagnostou, J. S. Barnet, S. M. Bohaty, D. De Vleeschouwer, F. Florindo, An astronomically dated record of Earth's climate and its predictability over the last 66 million years. *Science* **369**, 1383–1387 (2020).
121. L. B. Stap, C. J. Berends, R. S. W. van de Wal, Miocene Antarctic Ice Sheet area adapts significantly faster than volume to CO_2-induced climate change. *Clim. Past* **20**, 257–266 (2024).
122. B. Duncan, R. McKay, R. Levy, T. Naish, J. Prebble, F. Sangiorgi, S. Krishnan, F. Hoem, C. Clowes, T. Dunkley Jones, E. Gasson, C. Kraus, D. K. Kulhanek, S. R. Meyers, H. Moossen, C. Warren, V. Willmott, G. T. Ventura, J. Bendle, Climatic and tectonic drivers of late Oligocene Antarctic ice volume. *Nat. Geosci.* **15**, 819–825 (2022).
123. F. Fetterer, K. Knowles, W. Meier, M. Savoie, A. Windnagel. *Sea Ice Index, Version 2* [Data Set] (National Snow and Ice Data Center, 2016); https://doi.org/10.7265/N5736NV7.
124. A. H. Orsi, T. Whitworth III, W. D. Nowlin Jr., On the meridional extent and fronts of the Antarctic Circumpolar Current. *Deep-Sea Res. I Oceanogr. Res. Pap.* **42**, 641–673 (1995).
125. M. T. Taner, F. Koehler, R. Sheriff, Complex seismic trace analysis. *Geophysics* **44**, 1041–1063 (1979).
126. S. Vaughan, A simple test for periodic signals in red noise. *Astron. Astrophys.* **431**, 391–403 (2005).
127. M. Crucifix, palinsol: Insolation for palaeoclimate studies. R package version 0.93 (2016); https://CRAN.R-project.org/package=palinsol.

Acknowledgments: We thank D. De Vleeschouwer and the reviewers for their constructive feedback, which significantly improved this report. We also appreciate the insights of P. Sadler, C. Kelly, J. Williams, and B. Singer on an earlier version of the manuscript. Special thanks to G. Acton for his valuable contributions to the interpretation of paleomagnetic data from AND-2A. This work comprises part of N.B.S.'s dissertation, advised by S.R.M., and completed at the University of Wisconsin–Madison in 2022. **Funding:** This work was supported by the University of Wisconsin–Madison Cline-Pray-Dott Fund (N.B.S.), USSSP Schlanger Fellowship (N.B.S.), Guggenheim Fellowship and sabbatical leave (S.R.M.), National Science Foundation EAR 1151438 (S.R.M. and N.B.S.), Heising-Simons Foundation Award #2021-2797 (S.R.M. and N.B.S.), New Zealand Antarctic Science Platform Contract ANTA1801 (R.M.M., R.H.L., and G.E.G.), Royal Society of New Zealand Te Apārangi Marsden Fund Grant 18-VUW-089 (R.M.M.), Natural Environment Research Council (NERC) grant NE/W000172/1 (T.v.d.F. and J.M.), and Italian National Antarctic Research Program (PNRA) grant PNRA18-00233 (M.P.). **Author contributions:** Conceptualization: D.H., J.M., M.O.P., N.B.S., R.H.L., R.M.M., S.R.M., and T.R.N. Data curation: N.B.S. and S.R.M. Formal analysis: F.F., N.B.S., and S.R.M. Funding acquisition: N.B.S., R.M.M., and S.R.M. Investigation: F.T., L.D.S., L.Z., M.P., N.B.S., R.H.L., R.M.M., S.R.M., and F.F. Methodology: G.R.G., N.B.S., R.H.L., R.M.M., and S.R.M. Project administration: F.F., N.B.S., R.M.M., and S.R.M. Resources: S.R.M. and T.v.d.F. Software: G.R.G., N.B.S., and S.R.M. Supervision: N.B.S., R.M.M., and S.R.M. Validation: N.B.S., S.R.M., T.R.N., and T.v.d.F. Visualization: N.B.S., R.H.L., and S.R.M. Writing—original draft: N.B.S., R.H.L., and S.R.M. Writing—review and editing: F.F., J.M., L.Z., M.P., N.B.S., R.H.L., R.M.M., S.R.M., T.R.N., and T.v.d.F. **Competing interests:** The authors declare that they have no competing interests. **Data and materials availability:** All data needed to evaluate the conclusions in the paper are present in the paper and/or the Supplementary Materials.

Submitted 21 October 2023
Accepted 20 March 2025
Published 25 April 2025
10.1126/sciadv.adl1996